Open-Pit Mine Area Mapping With Gaofen-2 Satellite Images Using U-Net+

Tao Chen, *Senior Member, IEEE*, Xiaoxiong Zheng, Ruiqing Niu, and Antonio Plaza, *Fellow, IEEE*

***Abstract*—Obtaining information on the surface coverage of open-pit mining areas (OPMAs) is of great significance to ecological governance and restoration. The current methods to map the OPMAs face problems such as low mapping accuracy due to complex landscapes. In this article, we propose a hybrid open-pit mining mapping (OPMM) framework with Gaofen-2 (GF-2) high-spatial resolution satellite images (HSRSIs), using an improved U-Net neural network (U-Net+). By concatenating the previous layers with each subsequent layer to ensure that there is a maximum of feature maps of each layer in the network, the U-Net+ can reduce the loss of feature information and make the extraction capability of the network more powerful. Two independent OPMAs were selected as the study area for the OPMM. By taking advantage of GF-2 HSRSIs, a total of 111 open-pit mine sites (OPMSs) were mapped and each OPMS boundary was validated by field surveys. Then, these OPMSs were used as input to assess the accuracy of the OPMM results obtained by the U-Net+. By comparing our results with those provided by five state-of-the-art deep learning algorithms: Fully Convolutional Network (FCN), SegNet, U-Net, Residual U-Net (ResU-Net), and U-Net++, we conclude that the proposed framework outperformed these methods by more than 0.02% in Overall Accuracy, 0.06% in Kappa Coefficient, 0.03% in Mean Intersection over union, 8.36% in producer accuracy and 4.44% in user accuracy. Therefore, the proposed framework thus exhibits very promising applicability in the ecological restoration and governance of OPMAs.**

***Index Terms*—Deep learning, Gaofen-2 (GF-2), open-pit mine mapping, U-Net.**

Manuscript received December 12, 2021; revised March 3, 2022; accepted April 26, 2022. Date of publication April 29, 2022; date of current version May 13, 2022. This work was supported in part by the National Natural Science Foundation of China under Grant 62071439, and Grant 61871259, in part by the Opening Foundation of Qilian Mountain National Park Research Center (Qinghai) under Grant GKQ2019-01, in part by the Opening Foundation of Beijing Key Laboratory of Urban Spatial Information Engineering, under Grant 20210209, and in part by the Opening Foundation of Geomatics Technology and Application Key Laboratory of Qinghai Province, under Grant QHDX-2019-01. *(Corresponding author: Tao Chen.)*

Tao Chen is with the Institute of Geophysics and Geomatics, China University of Geosciences, Wuhan 430074, China, and with the Geomatics Technology and Application key Laboratory of Qinghai Province, Xining 810001, China, and also with the Beijing Key Laboratory of Urban Spatial Information Engineering, Beijing 100038, China (e-mail: taochen@cug.edu.cn).

Xiaoxiong Zheng is with the Institute of Geophysics and Geomatics, China University of Geosciences, Wuhan 430074, China, and also with Satellite Application Center for Ecology and Environment, Ministry of Ecology and Environment, Beijing 100094, China (e-mail: zbear@cug.edu.cn).

Ruiqing Niu is with the Institute of Geophysics and Geomatics, China University of Geosciences, Wuhan 430074, China (e-mail: niuruiqing@cug.edu.cn).

Antonio Plaza is with the Hyperspectral Computing Laboratory, Department of Technology of Computers and Communications, Escuela Politécnica, University of Extremadura, 10071 Cáceres, Spain (e-mail: aplaza@unex.es).

Digital Object Identifier 10.1109/JSTARS.2022.3171290

I. Introduction

MINERAL resources are of great significance for the survival and development of mankind. Since modern times, the exploitation and utilization of mineral resources has become more and more important. The open-pit mining areas (OPMAs) formed after mining destroyed the surface landscape and land resources, and caused ecological problems [1], [2] and geological disasters such as landslides [3]–[6]. To address this situation, researchers are paying more and more attention to the ecological restoration of OPMAs [7]. In the process of ecological restoration of mining areas, it is particularly important to obtain the distribution of ground features. In the early days, the ground feature information of the OPMAs was obtained through field surveys [8]. This method is not only time-consuming and labor-intensive, but it is also unsuitable to conduct whole-region surveys. High-spatial resolution satellite images (HSRSIs) can provide more clear surface information, and can achieve large-scale and rapid surface type coverage survey and monitoring [9]. Through remote sensing mapping of OPMAs, we can find out the classification of mining areas, effectively define the scope of ecological damage caused by mining, and provide basic data for ecological environment management and restoration in OPMAs. Therefore, it is feasible to use HSRSIs to obtain surface information in OPMAs.

Since the 1970s, remotely sensed data have been used for classification and mapping of ground features in OPMAs mainly based on visual interpretation, such as land cover information extraction [10], land use database establishment [11], land use mapping [12], [13], maximum likelihood [14], Model estimation [15], and long-term mining area changes analysis [16], [17]. The visual interpretation method reduces the cost of on-site investigation and improves the efficiency of open-pit mining mapping (OPMM), but it is still time-consuming, costly, and subjective, although the results are reliable. With the development of computer science, researchers have begun to adopt computer graphics techniques, such as gray-scale edge detection [18], to map the surface coverage in mining areas. In recent years, with the development of machine learning, scholars have gradually applied various machine learning algorithms to extract ground feature information in mining areas, such as decision trees [19], support vector machines (SVM) [20], and deep belief networks [21]. Although the machine learning methods achieve good results in OPMM, there are remain many unsolved problems due to the complex composition of ground features, and irregular spatial distributions in OPMAs.

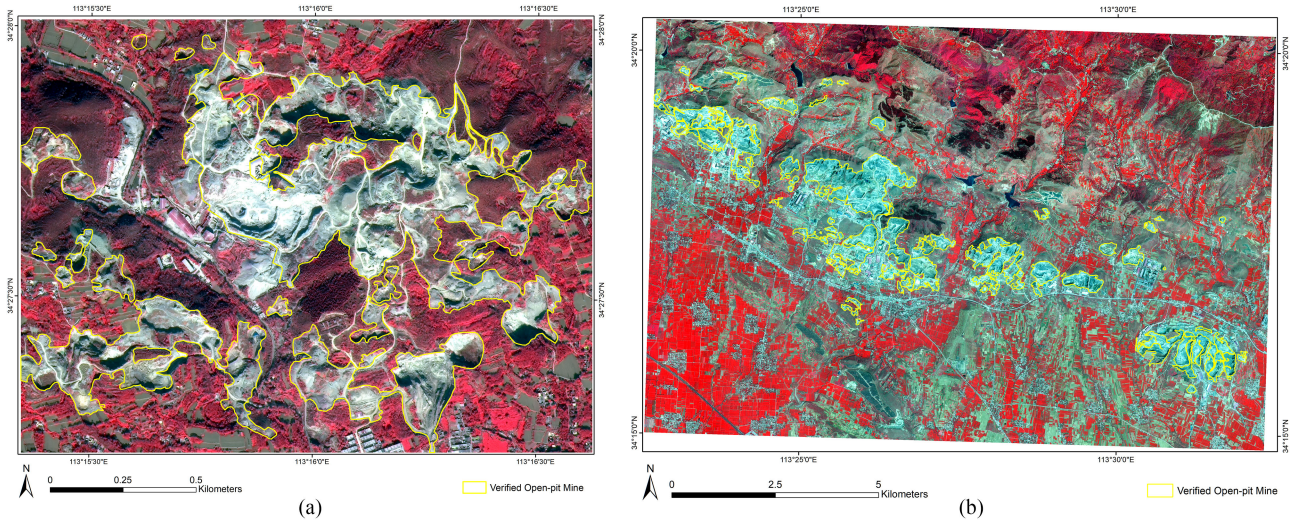

Fig. 1. Location of the study areas (R: Band4, G: Band3, B: Band2 of GF-2 HSRSIs). (a) Site 1: Dengfeng City. (b) Site 2: Yuzhou City.

In recent years, deep learning methods have become more and more popular in pattern recognition, especially in the field of image processing, including remote sensing images [22]. The most discriminative and representative features can be hierarchically learnt in end-to-end fashion [23]. Deep learning methods can extract the features of ground information through the training process, which intelligently completes the classification of the mining area and obtains a fine classification map of ground features without the need to manually design features or rules. The OPMA can be directly mapped after the remote sensing images of the open-pit mining area are classified by using the deep learning algorithm. Convolutional neural networks (CNNs) have been used in OPMM [24]. The CNN-based OPMM method outperforms traditional SVM based OPMM methods, but it still faces low efficiency and a poor performance due to the fact that it cannot process complicated large-scale HSRSIs.

Fully convolutional networks (FCNs) were proposed in 2014 [25] and were pivotal for end-to-end, pixel-level classification of images. The most popular semantic segmentation neural networks (SSNNs) are FCNs [25], SegNet [26], U-Net [27], ResU-Net [28], and U-Net++ [29]. These SSNNs exhibit good potential in many tasks, such as medical image processing and autonomous driving, but to the best of our knowledge, only a few models are used in OPMM [30]. Due to the network structural limitations, the accuracy of SSNNs in OPMM still needs to be further improved [31].

To address these issues, this article proposes a new OPMM framework based on Gaofen-2 (GF-2) HSRSIs, using an improved U-Net neural networks (U-Net+). The main contributions of our work can be summarized as follows: 1) An improved deep learning network U-Net+ with multilevel feature association is proposed, which can reduce the loss of feature information and make the extraction capability of the network more powerful by making sure a maximum of feature maps of each layer in the network; 2) The proposed U-Net+ is applied to the mapping of OPMAs, which improves the accuracy of mapping and can provide basic data for ecological environment governance.

The rest of this article is organized as follows. Section II introduces the data used in the work. Section III presents the methods compared in this article. Results and discussions are given in Section IV, followed by a summary in the last section.

II. Study Area and Data Sources

A. Study Area

In this study, two independent areas are selected as the study area. Site 1 is in Dengfeng City [Fig. 1(a)] while Site 2 is located in Yuzhou City, which is in the central part of Henan Province [Fig. 1(b)].

1) Site 1. Dengfeng City: The study area of Site 1 is located in the east of Dengfeng City, Henan Province, between 113°15'E to 113°17'E and 34°27'N to 34°28'N with an area of 2.9 km^2. The types of terrain in this area are mainly mountains and hills. The terrain in Dengfeng City gradually decreases from the north to south. The area is with a warm temperate continental monsoon, with bright sunshine and a clear distinction between the four seasons. Dengfeng City is rich in mineral resources, the main mineral are coal and aluminum mines. The Dengfeng City has a frequent crust activity, complex geological structure, and different rock metamorphosis, which create favorable conditions for the formation of multisample minerals in this city.

2) Site 2. Yuzhou City: The study area of Site 2 is in the east of Yuzhou City, Henan Province, between 113°22'E to 113°33'E and 34°14' to 34°21'with an area of 150 km^2. The terrain in Yuzhou City is high in northwest, and low in southeast. The area has a mainland monsoon climate, with four distinct seasons. It is located in the transitional zone between the Yudong Plain and the Funiu Mountain Range with a changing topography. Yuzhou City has a complex formation structure. Its mineral resources are rich with the main mineral deposits of coal, aluminum mines, iron, ceramic soil, and limestone. Since most of these mineral deposits are open-pit mining, the open-pit mining activities may cause a lot of environmental problems which conflicts with the Chinese government's green mining policy. This situation

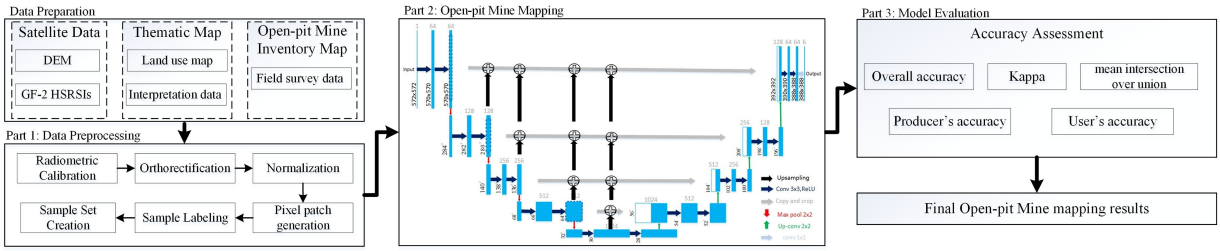

Fig. 2. Flowchart of the proposed U-Net+-based OPMM (UN+OPMM) framework.

makes the mapping of open-pit mine (OPM) necessary for the future studies and government decision makers to strengthen the ecological construction of mines.

B. Data Sources

Two GF-2 HSRSIs were used in this study. The first one was captured on October 30, 2017 for Dengfeng City, while the second one was captured on April 16, 2018 for Yuzhou City. GF-2 HSRSIs has four multispectral bands [blue (0.45∼0.52 μm), green (0.52∼0.59 μm), red (0.63∼0.69 μm), and near infrared (0.77∼0.89 μm)] with a spatial resolution of 4 m. Based on the land use map provided by the Geological Environmental Monitoring Institute of Henan Province, the land use types (LUTs) were classified into six domain groups, including OPM, buildings (BUI), bare soil (BAS), road (ROA), vegetation (VEG), and waste-dump area (WDA) in Site 1 and seven domain groups, including OPM, water (WAT), BUI, BAS, ROA, VEG, and WDA, in Site 2.

Open-pit mine sites (OPMSs) and boundaries in this study were first visually interpreted on GF-2 HSRSIs. Then, with the help of Geological Environmental Monitoring Institute of Henan Province, a sequence of field investigations was implemented from 27 August to 26 September 2018. After the field investigations, 16 OPMSs, which covered a total area of 0.93 km^2, were mapped in Site 1, accounting for 32.07% of the area of Site 1, while 95 OPMSs were mapped in Site 2, which covered an area of 10.1 km^2 in total, accounting for 6.73% of the area of Site 2. The largest area of OPM is 0.6 km^2 in Site 1 and 2.11 km^2 in Site 2 while the smallest one is 1514 m^2, in Site 1 and 1361 m^2 in Site 2. Finally, all the mapped OPMSs were subsequently digitized and rasterized into the same resolution (4 × 4 m) as the HSRSIs used for the study in Environmental Systems Research Institute's ArcGIS software (Version 10.3.0). In this study, after dicing the data from the two study areas, we randomly selected 70% as training data and 30% as validation data for experiments.

III. Methodology

The whole OPMM framework consists of three parts which is shown in Fig. 2. The first part is the data preprocessing workflow for image processing, and the preparation of OPMM training dataset is designed for the training samples generation. In data preprocessing stage, it mainly includes the optical image processing, and sample annotation. A sample set was created in this stage by using standardization and cutting operations. In the second part, an improved U-Net neural network (U-Net+) was used to mapping the OPM, which is the first-time that SSNNs used in the OPMM area. The third part is the model evaluation, in which we used several evaluation metrics to assess the performance of our proposed U-Net+ OPMM model (UN+OPMM) among five other common semantic segmentation networks: FCN-8s [25], SegNet [26], U-Net [27], ResU-Net [28], and U-Net++ [29].

A. Data Preprocessing

In the first step, a radiometric calibration was carried out through the radiometric calibration tool in Envi 5.3 software. Then an orthorectification progress was done to the radiometric calibrated images by combing the digital elevation model (DEM) data and using the RPC Orthorectification Workflow in Envi 5.3 software. After that, the image data were normalized to facilitate the training progress of the deep neural network, and the pixel patches were generated with a size of 512 × 512 pixels. By means of integration with the land use map, each pixel was labeled with a land use type, then the sample set was created for the deep neural network.

B. Fully Convolutional Neural Network (FCN)

CNNs solve the classification at the picture level, but cannot achieve the classification at the pixel level. If the classification of all pixels is carried out, it is necessary to construct an image block for each pixel first, and then classify the pixel block [32]. This method achieves pixel-level classification, but has some disadvantages such as data redundancy, excessive memory usage, large amount of calculations, and slow training speed, and the size of the image block is difficult to determine, which will affect the network's learning of information around the pixel and result in poor classification accuracy [25], [33]. FCNs were proposed to solve these problems [25]. FCNs replace the fully connected layer in the CNN with a convolutional layer, and introduces an upsampling layer in the network to achieve the same output structure and the size of the input image. According to the different upsampling multiples, FCN has three structures: FCN-8s, FCN-16s, and FCN-32s (Fig. 3). We selected FCN-8s as the FCN OPMM model in this study since it performs best among these three FCN models in most research tasks [25].

C. SegNet

SegNet is a symmetric network. There is an encoder and a corresponding decoder in the network, and the end of the network is a pixel-by-pixel classification layer [26]. The network

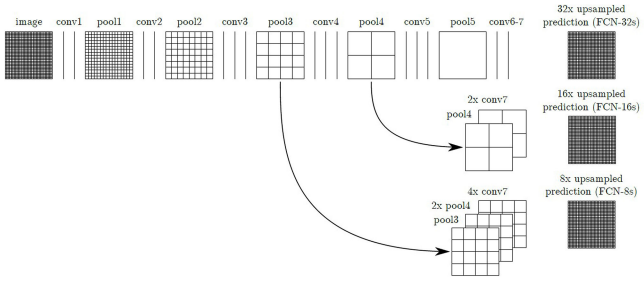

Fig. 3. Fully convolutional neural network structure.

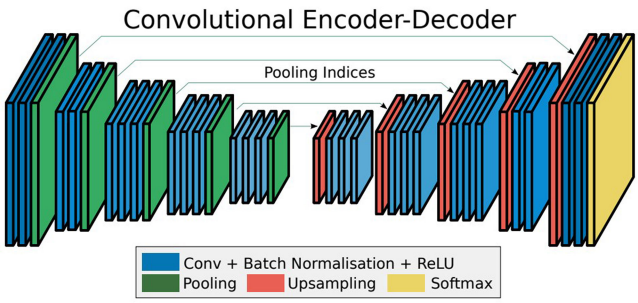

Fig. 4. Illustration of the SegNet architecture.

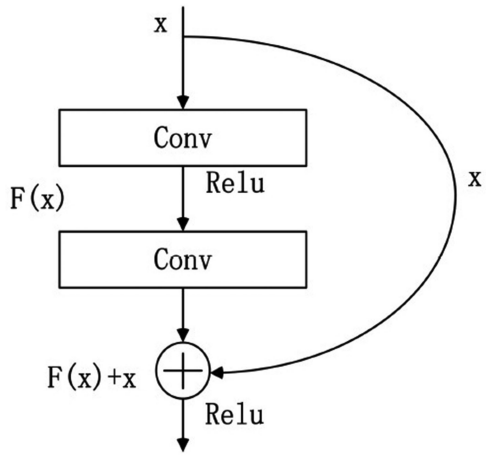

Fig. 5. Structure and principle of a residual block in ResU-Net.

structure of SegNet is shown in Fig. 4. The encoder network consists of 13 convolutional layers, corresponding to the first 13 convolutional layers in the VGG16 network [34], and uses the convolutional layer weights of the VGG network as the pre-training convolutional layer weights. The appropriate decoder in the decoder network uses the memory maximum pooling index from the corresponding encoder feature map to up-sample its input feature map.

D. ResU-Net

The ResU-Net model used in this article is improved based on U-Net by adding a residual block [35] between the various information extraction layers of the U-Net neural network to characterize the input information. Fig. 5 is a schematic diagram

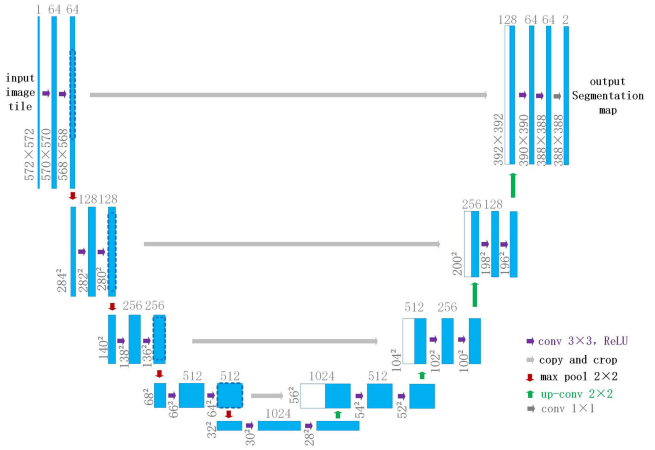

Fig. 6. Structure of ResU-Net.

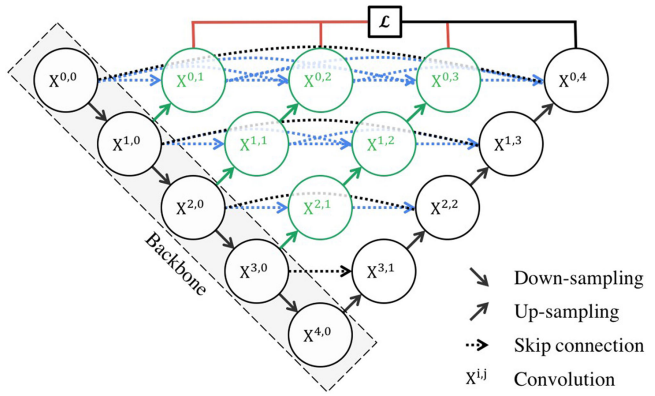

Fig. 7. Structure of U-Net++.

of the residual block. This method increases the number of layers of the network, which can solve the problem of gradient disappearance or gradient explosion, and ensures feature integrity [36]. The structure of ResU-Net is shown in Fig. 6.

E. U-Net++

Zhou *et al.* [29] proposed U-Net++ in 2018, which integrates more feature layer information by densely connecting and skip connecting the shallow feature layers in U-Net. The structure of U-Net++ is shown in Fig. 7.

F. U-Net+

As the depth of the network increases, after the information about the input and gradient passes through many layers, it may disappear gradually when it reaches the end (or the beginning) of the network [37]. Most networks reduce information loss by creating shortcuts between the previous and subsequent layers in the network [38]–[40]. The previous layers in the network will be concatenated with each subsequent layer. Through the cascade between the layers, the feature maps obtained from different layers in the network are combined to ensure that there is a maximum of each layer in the network, and then subsequent convolution operations are performed to reduce the

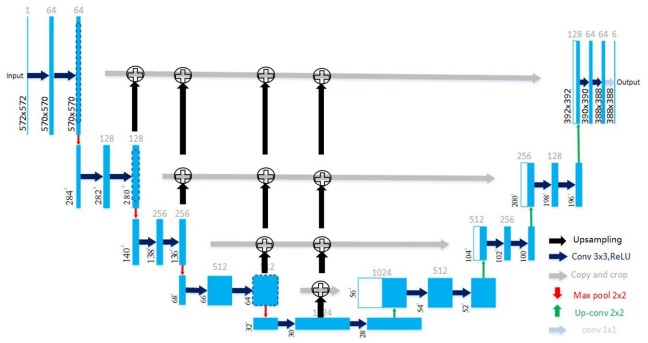

Fig. 8. Structure of U-Net+.

loss of feature information to a certain extent, making the feature extraction capability of the network more powerful. Inspired by the ResNet [28] and DenseNet [41], the network structure of the improved U-Net mainly performs one or more upsamplings of the feature layer obtained in the downsampling process, and expands to the same level of features. The size of the map is then used to add and sum the corresponding pixels in the way of adding, and integrate it into the up-sampling path to enhance the feature information of the network. The improved network structure is shown in Fig. 8, named U-Net+.

G. Evaluation Metrics

In order to evaluate the performance of our proposed UN+ OPMM model, six evaluation metrics (EMs): overall accuracy (OA), kappa coefficient (Kappa), mean intersection over union (mIoU), intersection over union (IoU), user's accuracy (UA), and producer's accuracy (PA) are used to analyze the mapping results [42]. The definition of each indicator is as follows.

1) OA: OA is the ratio of the number of correctly classified pixels to the total pixels, which represents the overall classification accuracy rate of the classification result. The formula is as follows, where P_t represents the number of pixels predicted to be the correct category, and L_n represents the total number of pixels.

$$\mathrm{OA} = P_t / L_n \times 100\%. \tag{1}$$

2) Kappa: Kappa is used in remote sensing image classification accuracy evaluation to judge the degree of agreement between the prediction result and the label [43]. N represents the total number of pixels, n is the number of classification categories, X_{ii} is the number of correctly classified pixels in the ith category, X_{i+} is the sum of the number of pixels in the column of the ith type, X_{+i} is the sum of the number of pixels in the row of the ith type. The calculation formula of Kappa coefficient is

$$\mathrm{Kappa} = \frac{N \sum_{t=1}^{n} X_{ii} - \sum_{t=1}^{n} X_{i+} X_{+i}}{N^2 - \sum_{t=1}^{n} X_{i+} X_{+i}}. \tag{2}$$

3) mIoU: mIoU is used to evaluate the degree of overlap between the classification result and the label, which is the average of Intersection over union (IoU).

TABLE I
PARAMETER SETTINGS OF THE SIX DIFFERENT NETWORKS

SSNNs	Depth	Special Construction	Activation Function	Loss Function
FCN	22	Conv2DTranspose	ReLU	Cross Entropy
SegNet	37	UpSampling	ReLU	Cross Entropy
U-Net	27	Concatenate	ReLU	Cross Entropy
ResU-Net	43	Resblock	ReLU	Cross Entropy
U-Net++	27	Concatenate	ReLU	Cross Entropy
U-Net+	27	Add	ReLU	Cross Entropy

4) UA: UA refers to the ratio of the total number of pixels correctly classified into a certain class to the total number of pixels classified into this class by the classifier in the entire image, and its calculation formula is as follows:

$$\mathrm{UA} = X_{ii} / X_{i+}. \tag{3}$$

5) PA: PA represents the ratio of the number of pixels that the classifier correctly classifies the pixels of the entire image into a certain category to the total number of true references for that category. The calculation formula is as follows:

$$\mathrm{PA} = X_{ii} / X_{+i}. \tag{4}$$

IV. RESULTS AND ACCURACY ASSESSMENT

A. Sample Set Construction and Parameters Setting

In total, 2393 samples patches with a size of 512 × 512 pixels are generated in the sample set. Training samples and validation samples are randomly selected according to a ratio of 7:3 with the sklearn module in the TensorFlow-Keras framework. After 20 epochs in the training process, the whole-area tests are done based on the model with the minimum loss and maximum accuracy. Then the confusion matrix is calculated and the prediction image are produced in the "Python-3.6" platform.

The parameter settings of the six different SSNNs are shown in Table I. In this study, the activation function of the six employed deep learning neural networks all select ReLU function, since it is one of the most effective and widely used activation functions in network construction. The ReLU function has two main advantages: one is it can overcome gradient disappearance and the other is that it can be used to train prediction methods more effectively [44]. The cross-entropy function is chosen as the loss function while the adaptive moment estimation (Adam) algorithm is the optimizer for its suitability for solving optimization problems with large-scale data and related parameters. The learning rate used in Adam's algorithm in this work is set to 0.0001.

The experiment environment in this study is a work station equipped with an Intel Xeon(R) Silver 4210R CPU @2.4GHZ×40, 128GB RAM, and Nvidia GeForce RTX 3090 graphics card. The OPMM models constructed in this study are all built in the Python programming language based on the TensorFlow-Keras deep learning framework.

TABLE II
EMs OF DIFFERENT MODELS (THE BOLDED AND UNDERLINED VALUE MEANS THE HIGHEST EMs OF THE ROW)

EMs	OPMM models	OPM (%)	WAT (%)	BUI (%)	BAS (%)	ROA (%)	VEG (%)	WDA (%)
PA/UA	FCOPMM	86.77/86.91	72.60/96.60	84.84/77.28	0.07/34.64	10.24/52.70	98.78/95.38	5.81/59.25
	SeOPMM	73.78/80.36	0.00/0.00	87.41/66.83	0.00/0.00	7.54/**97.86**	98.57/95.18	0.09/25.28
	UOPMM	95.10/**95.04**	**90.71**/97.81	**92.11**/94.84	77.48/**94.20**	**74.15**/85.20	99.42/98.67	**87.66**/**95.64**
	RUOPMM	78.17/90.49	80.84/90.90	84.35/82.83	33.04/59.78	52.11/73.63	98.63/96.68	57.92/51.55
	UN++OPMM	60.19/76.20	81.15/53.25	61.24/89.92	0.20/27.79	33.92/64.87	99.23/92.52	5.56/32.94
	UN+OPMM	**95.13**/94.92	88.46/**98.35**	91.41/**95.36**	**83.36**/91.63	67.69/89.30	**99.52**/**98.70**	85.26/92.41
IoU	FCOPMM	76.74	70.79	67.90	0.07	9.38	94.28	5.59
	SeOPMM	62.51	0.00	60.96	0.00	7.53	93.89	0.09
	UOPMM	**90.60**	**88.90**	**87.72**	73.95	**65.69**	98.10	**84.29**
	RUOPMM	72.23	74.78	71.80	27.04	43.92	95.40	37.50
	UN++OPMM	50.67	47.39	57.30	0.20	28.66	91.87	4.99
	UN+OPMM	90.52	87.17	87.51	**77.46**	62.61	**98.23**	79.68

B. OPMM Results and Analysis

In this section, the mapping results of six SSNN-based OPMM models which are FCN-based OPMM (FCOPMM), SegNet-based OPMM (SeOPMM), U-Net-based OPMM (UOPMM), ResU-Net-based OPMM (RUOPMM), U-Net++-based OPMM (UN++OPMM), and UN+OPMM are analyzed and discussed.

1) Site 1. Dengfeng City: Six LUTs are mapped in Site 1, which are OPM, BUI, BAS, ROA, VEG, and WDA (Fig. 9). The red color area in Fig. 9 is the OPM extracted by the six SSNN-based OPMM models. The black solid area shows the verified OPM.

From Fig. 9, we can see that, among these six SSNN-based OPMM methods, SeOPMM performs the worst while UN+OPMM performs the best. Except UN+OPMM, other five OPMM models missed or/and misclassified a lot of OPMs, especially in the northwest corner in Site 1. The mapping results of FCOPMM and SeOPMM are not satisfactory since there are many unmapped OPMs in Fig. 9(a) and (b). In particular, SeOPMM missed BAS, and some small OPMs. Many OPMs are misclassified into BUI. Same as SeOPMM, RUOPMM's performance was not satisfactory because some OPMs with large area was classified into several BUI and BAS, and some WDAs was misclassified into BUI and BAS, too. In Fig. 9(f), we can see that the mapping results of UN+OPMM are good with complete categories and accurate boundaries of all six LUTs, but with a misclassification of WAT, which should not be exist in Site 1.

2) Site 2. Yuzhou City: Seven LUTs are distributed in Site 2, including OPM, WAT, BUI, BAS, ROA, VEG, and WDA. The classification results are shown in Fig. 10. The performances of each model in Site 2 are better as they are in Site 1. Among these six OPMM results, SeOPMM performed the worst while UN+OPMM achieved the best performance, since SeOPMM missed WAT and BAS in Site 2 while the other five models mapped all the seven LUTs. From the point view of OPMM, all these six SSNN-based OPMM models can identify most of the OPMs, and can achieve satisfied results, which indicates the SSNN-based OPMM methods can be applied in OPMM. But for the details of OPMM, FCOPMM and SeOPMM missed some OPMs in the northwest and misclassified some OPMs in the south area in Site 2. RUOPMM has the lower omission error of OPMs in the in the northwest and lower commission error of OPMs in the south, but it misclassified some BAS into OPM in the northeast corner in Site 2. UN+OPMM has the best performance in mapping the OPMs, the OPMM results in Fig. 10 shows the complete boundary of each OPM with the lowest omission and commission error.

C. Accuracy Assessment

Six EMs are selected to assess the performance of these six SSNN-based OPMM models, which are OA, Kappa, mIoU, PA, UA, and IoU. The EMs of different models are shown in Fig. 11 and Table II.

In general, our proposed UN+OPMM model was more effective in the task of mapping all the seven LUTs, with the highest OA, and Kappa values, which means the UN+OPMM mapped a largest number of correct samples than that of the other five models classified. The OA values of the six models are all above 90%, which means these six models can classify LUTs accurately. Compared with OA, the Kappa coefficient are different for the Kappa coefficient of UN++OPMM, FCOPMM and SeOPMM are just 63.83%,76.47%, and 71.62%, while the Kappa coefficient of UOPMM, RUOPMM, and UN+OPMM are 80.23%, 93.1%, and 93.16%, respectively, indicating that our proposed UN+OPMM performs best among these six models. In terms of mIoU, the newly proposed UN+OPMM reaches 83.31%, which is 0.86% lower than the original U-Net, followed by RUOPMM, FCOPMM, and UN++OPMM, while SeOPMM has the lowest mIoU of 32.14%. The higher OA values but lower mIoU values of FCOPMM, SeOPMM, RUOPMM, and UN++OPMM shows the unstable mapping performance of the network.

From the perspective of PA and UA, although not every category of UN+OPMM achieved the highest value, the number of the highest values was relatively large, indicating that UN+OPMM performed more prominently in all models. Among these seven LUTs, the UA values are higher than PA values in BAS, ROA, and while the PA values are higher than UA values in VEG in all the six SSNN-based OPMM models. For OPM, the PA value is higher than UA value in UOPMM, and UN+OPMM while the value of PA is lower than that of UA in other four models. For WAT, the PA values are higher than UA values in UN++OPMM but lower in other five models. From the perspective of BUI, the values of PA are higher than that of UA in

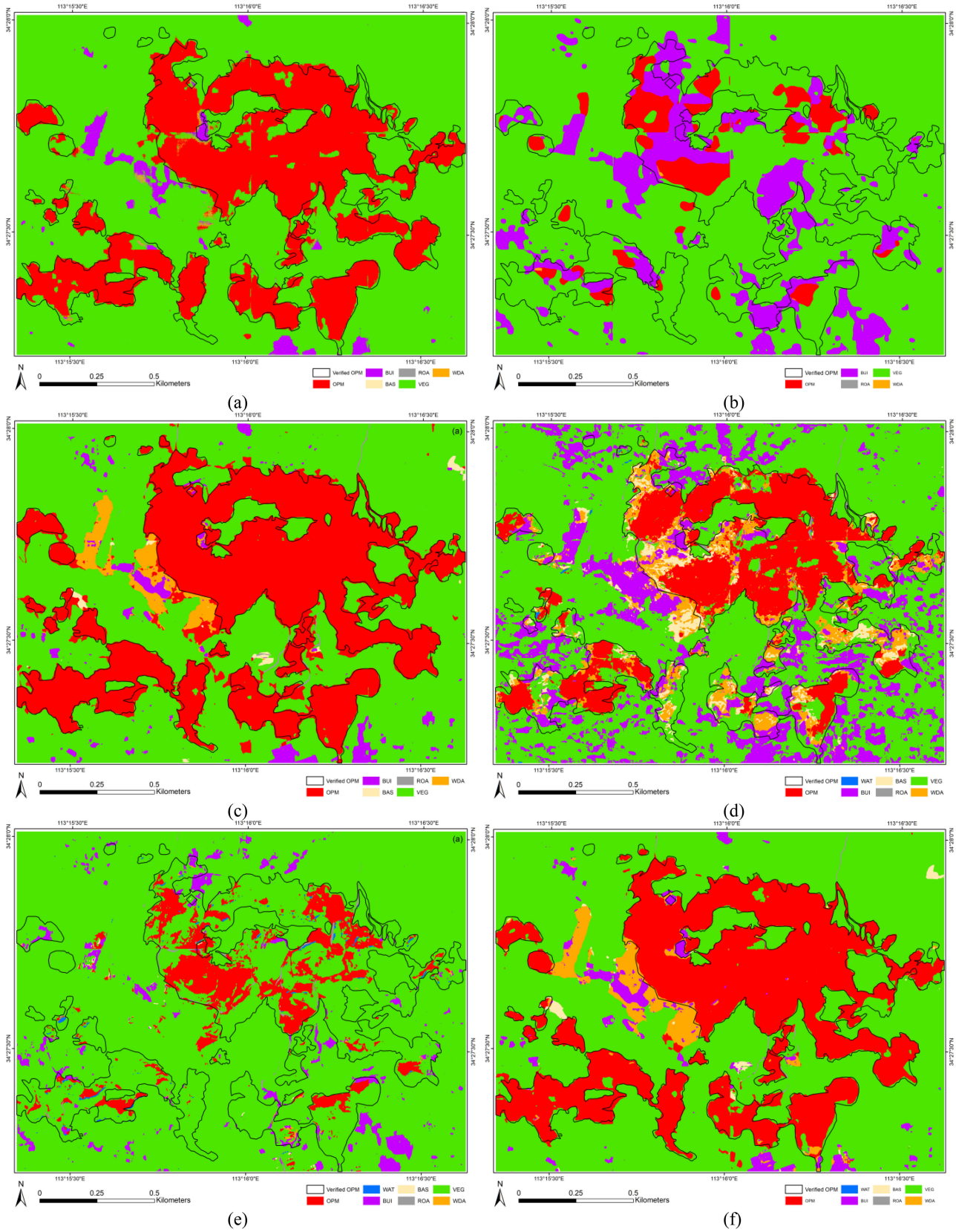

Fig. 9. OPMM results based on various SSNN-based OPMM methods in Site 1. (a) FCOPMM. (b) SeOPMM. (c) UOPMM. (d) RUOPMM. (e) UN++OPMM. (f) UN+OPMM.

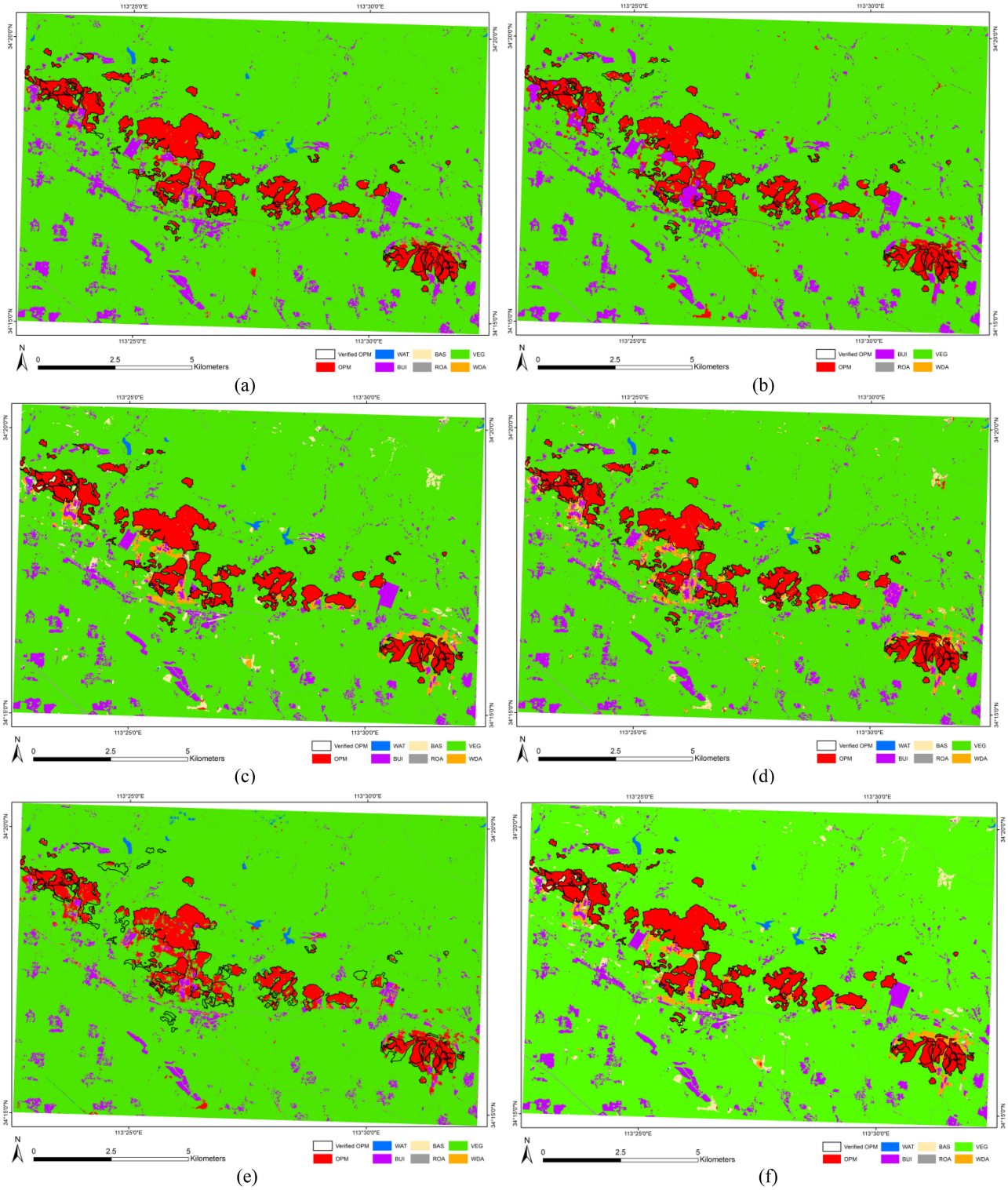

Fig. 10. OPMM results based on various SSNN-based methods in Site 2. (a) FCOPMM. (b) SeOPMM. (c) UOPMM. (d) RUOPMM. (e) UN++OPMM. (f) UN+OPMM.

three models (FCOPMM, SeOPMM, and RUOPMM) but lower in UOPMM, UN++OPMM, and UN+OPMM. For WDA, the PA values are higher than UA values only in RUOPMM but lower in other five models. A higher PA means that less objects were misclassified into other LUTs, and a higher UA means the number of mapped samples were more than that of total samples. As for IoU of each LUTs, the top two highest values are obtained by UOPMM, and UN+OPMM.

TABLE III
COMPLETION OF THE EVALUATION INDICATORS OF EACH MODEL

OPMM models	OA	Kappa	mIoU	PA/UA/IoU							Count
				OPM	WAT	BUI	BAS	ROA	VEG	WDA	
FCOPMM	×	×	×	×/×/×	×/×/×	×/×/×	×/×/×	×/×/×	×/×/×	×/×/×	0
SeOPMM	×	×	×	×/×/×	×/×/×	×/×/×	×/×/×	×/√/×	×/×/×	×/×/×	1
UOPMM	√	√	√	√/√/√	√/√/√	√/√/√	√/√/√	√/×/√	√/√/√	√/√/√	23
RUOPMM	×	×	×	×/×/×	×/×/×	×/×/×	×/×/×	×/×/×	×/×/×	×/×/×	0
UN++OPMM	×	×	×	×/×/×	×/×/×	×/×/×	×/×/×	×/×/×	×/×/×	×/×/×	0
UN+OPMM	√	√	√	√/√/√	√/√/√	√/√/√	√/√/√	√/√/√	√/√/√	√/√/√	**24**

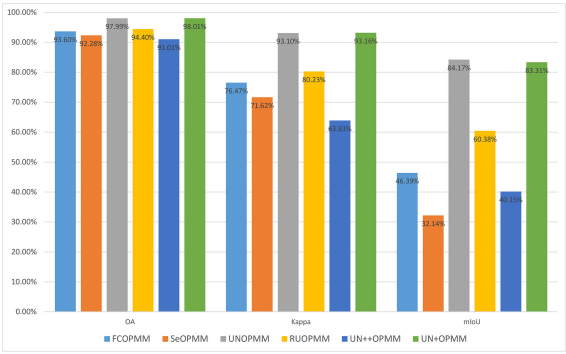

Fig. 11. OA, Kappa, and mIoU values of various SSNN-based methods.

D. Experimental Summary

The performance of each model is summarized and the results are shown in Table III. We considered a model successful when the six EM values achieved the top two in the experiment. We counted the performance of each model separately and summarized its number of successes.

It can be found that UN+OPMM performs stable in the six EMs since it reaches all top two accuracies among the six SSNN-OPMM model, indicating that our proposed UN+OPMM is more robust.

V. DISCUSSIONS

A. Factors Affecting the Mapping Accuracy

It is significant that UN+OPMM improves the mapping performance of all the seven LUTs of the OPMA. Among all the seven LUTs, the PA, UA, and IoU values of OPM type and VEG type are all above 90%. The main reason is that these two LUTs are the most common ones in Site 1 and Site 2, and their characteristics are obvious and easy to distinguish. The PA, UA, and IoU values of ROA, BAS, and WDA are all below 80%, especially for ROA, the PA and IoU values are below 70%, indicating that these three LUTs are not mapped well in Site 1 and Site 2, the main reasons are these three LUTs are less distributed and relatively dispersed in both two Sites. There are some similarities in the LUTs which caused by mining activities, such as OPM and WDA. These two LUTs can be easily confused since the composition of substances in WDA are extracted from the OPM. Also, the impact of the topography, landforms, and human activities within these two LUTs make it difficult to distinguish between them.

B. Uncertainties in OPMM

Some uncertainties still remain in this study although our newly proposed UN+OPMM model achieves promising results in these two Sites. First, the performance of the OPMM model depends on the number of samples. From Table III and Figs. 9–11, we can see that the more samples in the LUTs, the higher the EMs of mapping results. Second, in this work, different types of OPMs are not mapped individually when we applied the SSNN-based OPMM methods, which may cause uncertainty because for a large area of OPMA, the types of OPM are often different and should be treated differently. Last but not least, the inventory of OPMM in the study area is not complete and consistent. This insufficient information may also introduce uncertainties, since we may not recognize the newly OPMA in these two Sites in our existing OPM inventory datasets.

C. Limitations and Future Work

Since deep learning model which achieve good performance need a lot of samples for training, the sample numbers and labeling becomes the first and biggest problem. In Fig. 10, we can see that, for the LUTs which are less distributed, we obtain the lowest EMs (ROA, BAS). So, the ability of the model to deal with a small number of samples in OPMM is an issue that needs to be addressed.

VI. CONCLUSION

In this article, we propose a hybrid SSNN-based OPMM framework for GF-2 HSRSIs by using UN+OPMM model, which was constructed by concatenating the previous layers with each subsequent layer, so that there is a maximum of feature maps of each layer in the network, which can reduce the loss of feature information and make the extraction capability of the network more powerful. A sample set of 2393 sample patches with a size of 512 × 512 pixels are generated, with a ratio of 7:3 of training samples and validation samples. The results of UN+OPMM are compared with five state-of-the-art deep learning algorithms: FCN, SegNet, U-Net, ResU-Net, and U-Net++. The results show that the proposed framework outperforms the original U-Net by 0.02% in OA, 0.06% in Kappa, and 0.03% in PA of OPMs, achieving higher accuracy than the other four methods. It can be concluded that the proposed framework exhibits promising performance in ecological restoration and governance of OPMAs.

REFERENCES

[1] D. Zhu, T. Chen, Z. Wang, and R. Niu, "Detecting ecological spatial-temporal changes by remote sensing ecological index with local adaptability," *J. Environ. Manage.*, vol. 299, Dec. 2021, Art. no. 113655.

[2] D. Zhu, T. Chen, N. Zhen, and R. Niu, "Monitoring the effects of open-pit mining on the eco-environment using a moving window-based remote sensing ecological index," *Environ. Sci. Pollut. Res.*, vol. 27, no. 13, pp. 15716–15728, Feb. 2020.

[3] S. Sengupta, A. P. Krishna, and I. Roy, "Slope failure susceptibility zonation using integrated remote sensing and GIS techniques: A case study over Jhingurdah open pit coal mine, Singrauli Coalfield, India," *J. Earth Syst. Sci.*, vol. 127, no. 6, Aug. 2018, Art. no. 82.

[4] T. Liu, T. Chen, R. Niu, and A. Plaza, "Landslide detection mapping employing CNN, ResNet, and DenseNet in the Three Gorges Reservoir, China," *IEEE J. Sel. Topics Appl. Earth Observ. Remote Sens.*, vol. 14, pp. 11417–11428, Oct. 2021.

[5] X. Gao, T. Chen, R. Niu, and A. Plaza, "Recognition and mapping of landslide using a fully convolutional DenseNet and influencing factors," *IEEE J. Sel. Topics Appl. Earth Observ. Remote Sens.*, vol. 14, pp. 7881–7894, Aug. 2021.

[6] H. Cai, T. Chen, R. Niu, and A. Plaza, "Landslide detection using densely connected convolutional networks and environmental conditions," *IEEE J. Sel. Topics Appl. Earth Observ. Remote Sens.*, vol. 14, pp. 5235–5247, May 2021.

[7] M. Toktar, G. Lo Papa, F. E. Kozybayeva, and C. Dazzi, "Ecological restoration in contaminated soils of Kokdzhon phosphate mining area (Zhambyl region, Kazakhstan)," *Ecological Eng.*, vol. 86, pp. 1–4, Nov. 2016.

[8] W. Chen, X. Li, H. He, and L. Wang, "A review of fine-scale land use and land cover classification in open-pit mining areas by remote sensing techniques," *Remote Sens.*, vol. 10, no. 1, Dec. 2017, Art. no. 15.

[9] X. X. Zheng and T. Chen, "High spatial resolution remote sensing image segmentation based on the multiclassification model and the binary classification model," *Neural Comput. Appl.*, pp. 1–8, 2021, doi: 10.1007/s00521-020-05561-8.

[10] B. Felinks, M. Pilarski, and G. Wiegleb, "Vegetation survey in the former brown coal mining area of eastern Germany by integrating remote sensing and ground-based methods," *Appl. Vegetation Sci.*, vol. 1, no. 2, pp. 233–240, Feb. 1998.

[11] J. E. Vogelmann *et al.*, "Completion of the 1990s national land cover data set for the conterminous United States from Landsat thematic mapper data and ancillary data sources," *Photogrammetric Eng. Remote Sens.*, vol. 67, no. 6, pp. 650–662, Jun. 2001.

[12] J. Nan, Z. Zhao, Y. Hong, and R. Du, "Remote sensing investigation of coal mines in Xuanwei of Yunnan province for their development," *Remote Sens. Land Resour.*, vol. 31, no. 8, pp. 121–124, Jun. 2012.

[13] A. Prakash and R. P. Gupta, "Land-use mapping and change detection in a coal mining area—A case study in the Jharia Coalfield, India," *Int. J. Remote Sens.*, vol. 19, no. 3, pp. 391–410, 1998.

[14] J. R. Irons and R. L. Kennard, "The utility of thematic mapper sensor characteristics for surface mine monitoring," *Photogramm. Eng. Remote Sens.*, vol. 52, no. 3, pp. 389–396, Mar. 1986.

[15] E. E. Duncan, J. S. Kuma, and S. Primpong, "Open pit mining and land use changes: An example from Bogosu-Prestea area, South West Ghana," *Electron. J. Inf. Syst. Developing Countries*, vol. 36, no. 1, pp. 1–10, 2009.

[16] A. H. Bangian, M. Ataei, A. Sayadi, and A. Gholinejad, "Optimizing post-mining land use for pit area in open-pit mining using fuzzy decision making method," *Int. J. Environ. Sci. Technol.*, vol. 9, no. 4, pp. 613–628, 2012.

[17] H. Zeng, Z. Hu, and H. Xie, "Research on LUCC information atlas based on multi-temporal remote sensing in coal mining area," *J. Liaoning Tech. Univ.*, vol. 26, no. 4, pp. 626–629, Aug. 2007.

[18] P. Du, L. Yuan, J. Xia, and J. He, "Fusion and classification of Beijing-1 small satellite remote sensing image for land cover monitoring in mining area," *Chin. Geographical Sci.*, vol. 21, no. 6, pp. 656–665, 2011.

[19] A. E. Maxwell, T. A. Warner, and M. P. Strager, "Combining rapideye satellite imagery and lidar for mapping of mining and mine reclamation," *Photogrammetric Eng. Remote Sens.*, vol. 80, no. 2, pp. 179–189, Feb. 2014.

[20] W. Chen, X. Li, and L. Wang, "Fine land cover classification in an open pit mining area using optimized support vector machine and worldview-3 imagery," *Remote Sens.*, vol. 12, no. 1, Dec. 2019, Art. no. 82.

[21] M. Li *et al.*, "A multi-level output-based DBN model for fine classification of complex geo-environments area using Ziyuan-3 TMS imagery," *Sensors*, vol. 21, no. 6, Mar. 2021, Art. no. 2089.

[22] N. Kussul, M. Lavreniuk, S. Skakun, and A. Shelestov, "Deep learning classification of land cover and crop types using remote sensing data," *IEEE Geosci. Remote Sens. Lett.*, vol. 14, no. 5, pp. 778–782, May 2017.

[23] Y. Chen, H. Jiang, C. Li, X. Jia, and P. Ghamisi, "Deep feature extraction and classification of hyperspectral images based on convolutional neural networks," *IEEE Trans. Geosci. Remote Sens.*, vol. 54, no. 10, pp. 6232–6251, Oct. 2016.

[24] T. Chen, N. Hu, R. Niu, N. Zhen, and A. Plaza, "Object-oriented open-pit mine mapping using Gaofen-2 satellite image and convolutional neural network, for the Yuzhou City, China," *Remote Sens.*, vol. 12, no. 23, Nov. 2020, Art. no. 3895.

[25] J. Long, E. Shelhamer, and T. Darrell, "Fully convolutional networks for semantic segmentation," *IEEE Trans. Pattern Anal. Mach. Intell.*, vol. 39, no. 4, pp. 640–651, Apr. 2017.

[26] V. Badrinarayanan, A. Kendall, and R. Cipolla, "SegNet: A deep convolutional encoder-decoder architecture for image segmentation," *IEEE Trans. Pattern Anal. Mach. Intell.*, vol. 39, no. 12, pp. 2481–2495, Dec. 2017.

[27] O. Ronneberger, P. Fischer, and T. Brox, "U-Net: Convolutional networks for biomedical image segmentation," *Lecture Notes Comput. Sci.*, vol. 9351, pp. 234–241, Nov. 2015.

[28] X. Xiao, L. Shen, and Z. Luo, "Weighted Res-UNet for high-quality retina vessel segmentation," in *Proc. 9th Int. Conf. Inf. Technol. Med. Educ.*, Oct. 2018, pp. 327–331.

[29] Z. Zhou, M. M. Rahman Siddiquee, N. Tajbakhsh, and J. Liang, "UNet++: A nested U-net architecture for medical image segmentation," in *Deep Learning in Medical Image Analysis and Multimodal Learning for Clinical Decision Support*. Cham, Switzerland: Springer, 2018, pp. 3–11.

[30] H. Xie, Y. Pan, J. Luan, X. Yang, and Y. Xi, "Open-pit mining area segmentation of remote sensing images based on DUSegNet," *J. Indian Soc. Remote*, vol. 49, no. 6, pp. 1257–1270, Feb. 2021.

[31] Y. Song, J. Dong, Y. Huang, and H. Wan, "Research on the priority of the land use types extraction of opencast mine area based on object-oriented classification," *Remote Sens. Technol. Appl.*, vol. 31, no. 3, pp. 572–579, Jun. 2016.

[32] G. Sumbul and B. Demir, "A novel multi-attention driven system for multi-label remote sensing image classification," in *Proc. IEEE Int. Geosci. Remote Sens. Symp. (IGARSS)*, 2019, pp. 5726–5729.

[33] C. Li, P. Qin, and J. Zhang, "Research on image denoising based on deep convolutional neural network," *Comput. Eng.*, vol. 43, no. 3, pp. 253–260, Mar. 2017.

[34] K. Simonyan and A. Zisserman, "Very deep convolutional networks for large-scale image recognition," 2015, *arXiv:1409.1556*.

[35] K. He, X. Zhang, S. Ren, and J. Sun, "Deep residual learning for image recognition," in *Proc. Comput. Vis. Pattern Recognit.*, 2016, pp. 770–778.

[36] P. Liu, Y. Wei, Q. Wang, Y. Chen, and J. Xie, "Research on post-earthquake landslide extraction algorithm based on improved U-Net model," *Remote Sens.*, vol. 12, no. 5, Mar. 2020, Art. no. 894.

[37] P. Le and W. Zuidema, "Quantifying the vanishing gradient and long distance dependency problem in recursive neural networks and recursive LSTMs," 2016, *arXiv:1603.00423*.

[38] B. Lee, S. Son, H. Kim, S. Nah, and K. Lee, "Enhanced deep residual networks for single image super-resolution," in *Proc. Comput. Vis. Pattern Recognit.*, 2017, pp. 136–144.

[39] H. Chen, Q. Dou, L. Yu, J. Qin, and P. A. Heng, "VoxResNet: Deep voxelwise residual networks for brain segmentation from 3D MR images," *NeuroImage*, vol. 170, pp. 446–455, Apr. 2018.

[40] P. L. Bartlett, D. P. Helmbold, and P. M. Long, "Gradient descent with identity initialization efficiently learns positive-definite linear transformations by deep residual networks," *Neural Comput.*, vol. 31, no. 3, pp. 477–502, Mar. 2019.

[41] G. Huang, Z. Liu, L. van der Maaten, and K. Q. Weinberger, "Densely connected convolutional networks," in *Proc. Comput. Vis. Pattern Recognit.*, 2017, pp. 4700–4708.

[42] G. Csurka, D. Larlus, F. Perronnin, and F. Meylan, "What is a good evaluation measure for semantic segmentation?," in *Proc. 24th Brit. Mach. Vis. Conf.*, 2013, vol. 2013, pp. 10–5244.

[43] J. Cohen, "A coefficient of agreement for nominal scaler," *Educ. Psychol. Meas.*, vol. 20, pp. 37–46, 1960.

[44] N. Tong, M. Cao, and K. Sheng, "Shape constrained fully convolutional DenseNet with adversarial training for multi-organ segmentation on head and neck low field MR images," *Int. J. Radiat. Oncol. Biol. Phys.*, vol. 105, no. 1, pp. S93–S93, Sep. 2019.

Tao Chen (Senior Member, IEEE) received the Ph.D. degree in photogrammetry and remote sensing from Wuhan University, Wuhan, China, in 2008.

From 2015 to 2016, he was a Visiting Scholar with the University of New South Wales, Sydney, Australia. He has authored or coauthored more than 50 scientific papers including IEEE JOURNAL OF SELECTED TOPICS IN APPLIED EARTH OBSERVATIONS AND REMOTE SENSING, *Journal of Environmental Management*, *Remote Sensing*, *Environmental Earth Sciences*, and *Environmental Science and Pollution Research*, and guest edited two journal special issues. His research interests include image processing, machine learning, and geological remote sensing.

Xiaoxiong Zheng received the M.S. degree in geological engineering from China University of Geosciences, Wuhan, China, in 2021.

He is currently with the Satellite Environment Application Center of the Ministry of Ecology and Environment. His current main research interests include remote sensing image classification based on deep learning.

Ruiqing Niu received the Ph.D. degree in earth exploration and information technology from the China University of Geosciences, Wuhan, China, in 2005.

He is currently a Full Professor with the Institute of Geophysics and Geomatics, China University of Geosciences. His research interests include remote sensing, geographic information system, and engineering geology.

Antonio Plaza (Fellow, IEEE) received the M.Sc. and Ph.D. degrees in computer engineering from the Department of Technology of Computers and Communications, University of Extremadura, Badajoz, Spain, in 1999 and 2002, respectively.

He is currently a Full Professor and the Head of the Hyperspectral Computing Laboratory, Department of Technology of Computers and Communications, University of Extremadura. He has authored more than 600 publications and guest edited ten journal special issues. He has reviewed more than 500 manuscripts for over 50 different journals.

Dr. Plaza served as the Editor-in-Chief for IEEE TRANSACTIONS ON GEOSCIENCE AND REMOTE SENSING from 2013 to 2017. He is included the Highly Cited Researchers List (Clarivate Analytics) from 2018 to 2020.